Imaging Pyrometry and Shock Wave Tracking During Ballistic Impact of Metal Projectiles

Dihia Idrici, Samuel Goroshin, David L. Frost
McGill University, Mechanical Engineering Department,
Montreal, Quebec, Canada

Zoe Laing, Jason Loiseau,
Royal Military College, Chem. and Chem. Engineering Department,
Kingston, Ontario, Canada

1   Introduction

The supersonic impact of a reactive metal projectile with a rigid target is a complex multistage process involving chemical energy release. Of particular interest is the period of contact between the projectile and the target, which can span a few microseconds. The early-impact stage is notable because (1) it is responsible for prompt (microsecond timescale) energy release, and (2) it is a precursor to the longer timescale chemical energy release during the post-impact stage [1]. In terminal ballistics, the study of the longer timescale energy release is typically done using the vented chamber calorimetry technique. The pressure rise inside the chamber is monitored to infer the total energy release and energy release efficiency [2]. To determine the mechanisms responsible for prompt energy release during the early-impact stage necessitates direct observation of the event, which requires the use of optical diagnostics with sub-microsecond time resolution.

In a study being conducted in parallel, we are investigating the sources that contribute to the formation of an impact blast wave. The present study is specifically concerned with the effect of chemical energy release on the strength of the blast wave. Pure reactive metal projectiles (Mg, Al, Ti, and Zr) are launched and impact a rigid target made of aluminum oxide at impact speeds between 1 to 1.3 km/s. The impacts are conducted in atmospheres with different oxygen concentrations, i.e., pure argon, binary mixtures of argon and oxygen (21%, 30%, and 40%), and air for reference. Three-colour imaging pyrometry with short exposure times (200 ns) is used to obtain the spatial temperature distribution of the metal particles to determine their combustion regime. A Shimadzu HPV-X2 high-speed camera is used to track the blast wave produced on impact, to estimate its speed or Mach number.

2   Experimental Setup

In the present work, a single-stage helium-driven light-gas gun (7.1 mm ID, 2.1 m long) is used to accelerate cylindrical projectiles (3.125 mm dia x 3.125 mm long) made of high purity (99.5%, Alfa

Aesar) Mg, Al, Ti, and Zr. Each projectile is lightly glued to the front of a 4.8-mm-thick polycarbonate sabot with a Bridgman seal machined at the rear face and a small Neodymium magnet embedded on the side. The impact velocities range between 1 – 1.3 km/s, which are characteristic of material velocities from explosively-launched projectiles. The impact target consists of a dense (3.9 g/cm^3) 50-mm-square, 10-mm-thick inert aluminum oxide plate, so the particles and fragments that are observed are from the projectile alone.

A representative schematic and description of the light-gas gun and test section can be found in [1]. A gas-dynamic sabot stripper was added after the double coil gauge to strip the sabot from the projectile so that the early-impact stage is not disrupted by the arrival of the sabot. The sabot stripper consists of a small volume of N$_2$ gas at a pressure of 2 atm contained between two 2 mil mylar diaphragms. Before each impact, the barrel is evacuated to facilitate the acceleration of the sabot-supported projectile. The impact occurs in a test section with opposing rectangular polycarbonate windows which allows optical access to visualize the impact process. The gun barrel and the test section together form a sealed system. However, each can be evacuated and filled with a gas independently.

3   Imaging Pyrometry

Three-colour imaging pyrometry is achieved by modifying an HSFC-Pro (PCO) imaging system, which consists of three monochrome cameras with intensifiers (three channels). The light from the impact event is collected through a common lens (AF-S Nikkor 300 mm) and is divided among the three different channels by a series of beam splitters. Behind each beam splitter is a narrow bandpass filter, followed by an image intensifier (photomultiplier, microchannel plate, and phosphor screen), and a CCD screen. A schematic of the experimental setup including the imaging pyrometer is shown in Fig. 1**.**
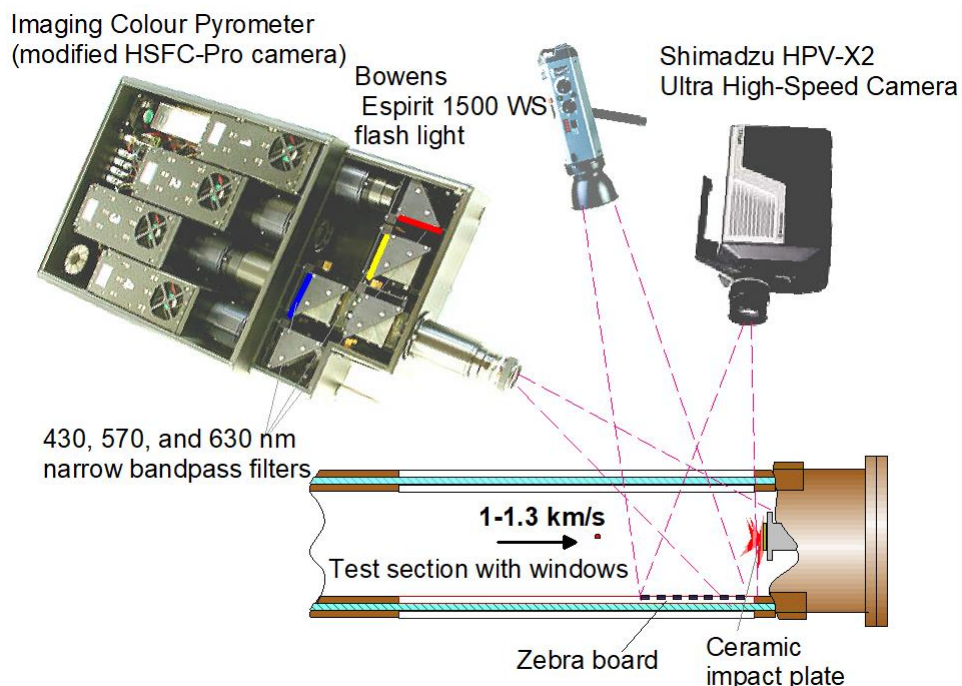

Fig. 1: Schematic of the experimental setup. The fourth camera of the imaging pyrometer is not used. Note that the flash is exclusively used in experiments where the impact blast wave is tracked

Each channel of the HSFC-Pro can only capture 2 images per impact event. However, two key advantages of the HSFC-Pro are that the exposure time can be set as low as 20 ns and the intensifiers permit the use of low exposure times when using small projectiles. The narrow bandpass filters used are

centered at 430, 570, and 630 nm ($\pm$ 2 nm) with a FWHM of 10 nm (Andover Corporation, 50 mm in dia.). The filter wavelengths fall outside any atomic lines and molecular bands that have been observed using emission spectroscopy with the four metals of interest, particularly the strong blue - green $X^2\Sigma^+ - B^2\Sigma^+$ AlO molecular band for Al combustion.

A modified SLR camera with a fiber taper bundle mounted on its film plane is used to collect light from the impact event and carry it via an optical fiber to a three-colour pyrometer described in [1]. The signals are recorded by an oscilloscope. One of the signals is used to trigger the imaging pyrometer and the Shimadzu camera.

3.1 Image Correction Procedure

All three camera channels of the imaging pyrometer have different optical paths. Consequently, they capture slightly different images. The main disadvantage of using three monochrome cameras with narrow bandpass filters over a colour camera with a triple-pass optical filter [3] is the necessity and difficulty of aligning with precision all three images. A software approach was adopted to correct for image distortion [4] as it is not recommended to fine tune the position of the optical components inside the HSFC-Pro. Image correction is carried out by imaging the target with fiducial markers applied to it before the impact. MATLAB's similarity transform function, from the image processing Toolbox, is used to map the images produced by cameras 1 and 2 onto the image produced by camera 3. The resulting image transformation matrices are used to correct the impact images.

3.2 Pyrometry

Pyrometry relies on Planck's law of radiation for black bodies to estimate the temperature of a condensed phase emitter. For the range of temperatures (500 – 4000 K), and the range of visible wavelengths under consideration, Wien's approximation to Planck's law is applied such that the dependence of spectral intensity (I) on wavelength (λ_i) and temperature (T) becomes:

$$I(\lambda_i, T) = \frac{C_1 \varepsilon(\lambda_i, T)}{\lambda_i^5} e^{-C_2/\lambda_i T} \qquad (1)$$

Where $C_1 = 1.199 \times 10^{-16}$ Wm^2 and $C_2 = 1.4388 \times 10^{-2}$ mK, and $\varepsilon(\lambda_i, T)$ is the emissivity of the solid. Within the 200 nm wavelength range under study, the gray body assumption is used [5, 6], where the emissivity of the metal is treated as a weak function of wavelength ($\varepsilon(T)$). The subscript i =1,2, and 3 refers to the three channels with wavelength 630, 570, and 430 nm, respectively. Expression (1) can be reformulated into a linear equation of the form $y = b + mx$ [3]:

$$\ln\left(I_{\lambda_i,T}\lambda_i{}^5\right) = \ln(C_1\varepsilon(T)) + \left(-\frac{C_2}{T}\right)\frac{1}{\lambda_i} \qquad (2)$$

For a gray body, a plot of $\ln\left(I_{\lambda_i,T}\lambda_i^5\right)$ vs $1/\lambda_i$ should be linear with a slope equal to $-\frac{C_2}{T}$ from which the temperature of the condensed phase can be extracted. A line fitting algorithm can be used to find the slope of the best fit line for the three data points at every pixel location. This method does not account for the Gaussian distribution of the light passing through the narrow bandpass filter centered at λ_i [4]. Both methods were tested, and both led to effectively the same results.

A) Calibration Light Source

The spectral response of each channel depends on wavelength. Therefore, for a pair of wavelengths, the pixel intensity ratio is most likely not equal to the true intensity ratio emitted by the hot object. The Thorlabs SLS201L filament tungsten-halogen lamp was used to calibrate the spectral response of the complete optical system (polycarbonate windows, lens, filters, and the three channels). This lamp has an approximate colour temperature of 2796 K and Thorlabs provides a data sheet of the normalized theoretical spectrum of the lamp, which accounts for the variance in emissivity with wavelength. The tungsten lamp was connected to a 1-mm-multimode optical fiber to mix the light. The other end of the

fiber was imaged by each channel at the same exposure time. The coefficients of calibration $\left(\gamma_{\lambda_i}\right)$, or correction factors, equal to the ratio of the theoretical relative intensity (provided by ThorLabs, $I_{\lambda_i,W}$) and the experimentally measured intensity ($I_{\lambda_i,E,W}$), are obtained using a procedure similar to the one described in [3, 4].

B) Sensitivity / Dynamic Range

To be able to detect variations in temperature, the ratios between corrected intensities should show a strong dependence on temperature [3]. With the filters selected, the imaging pyrometer has a higher sensitivity between 2000 – 3500 K which is adequate when combustion is involved.

C) Linear Response

In addition to temperature sensitivity, each channel must record an average pixel intensity that increases linearly with exposure time for a given light source. Linearity is obtained for all three channels above exposure times of $100\ \mu s$. At shorter exposure times, one or more of the images of the tungsten lamp were too faint to be useful. Linearity of the signal translates into nearly constant intensity calibration ratios, or sensitivity ratios, between channel pairs defined as $\sigma_{i,j} = \frac{\gamma_{\lambda_i}}{\gamma_{\lambda_j}}$.

The experimental exposure times are set to 200 ns, and in some cases $1\ \mu s$ for impacts in argon. To further validate the intensity calibration ratios at short exposure times, further tests are being carried out with a brighter calibration lamp (UIS-LS from StellarNet Inc.) and the results will be reported.

4   Blast Wave Tracking

To visualize the blast wave produced upon impact, a high-speed Shimadzu HPV-X2 camera operating at 1 Mframes/second is used with background lighting from a flash (Bowens Esprit 1500 WS). To enhance the visibility of the blast wave, a Zebra-board backdrop was used, consisting of alternating black and white stripes with a small angle. During the blast tracking experiments, imaging pyrometry was not used due to the background lighting. The flash was triggered with a signal sent by the double coil gauge, while the Shimadzu camera was triggered with the impact flash.

The data is analyzed using an in-house code which involves image processing to enhance the visibility of the blast and an open-source edge detection algorithm in MATLAB. The cylindrical projectiles impacted the target with a tilt angle that varied from one impact test to the next, which influenced the shape of the blast wave. In this paper we track specifically the trajectory of the blast wave at the horizontal level of the impact point and fit the position vs. time data to the fit used by Kleine et al. [7]. The function is then differentiated to determine the blast velocity and normalized (Mach number) to account for the change in sound speed.

5   Results and Discussion

Fig. 2 shows a sequence of events captured by the Shimadzu camera. (1) The projectile is moving from right to left towards the target with a leading bow shock. (2) An impact flash is observed upon contact of the projectile with the target. (3) A primary jet of bright metallic particles emerges from the interface between the projectile and the target. Its direction is determined by the tilt of the projectile. (4) A blast wave is observed to emerge, moving away from the impact point. Its shape is influenced by the direction of the particle jetting. Those features are common to all metals of interest.
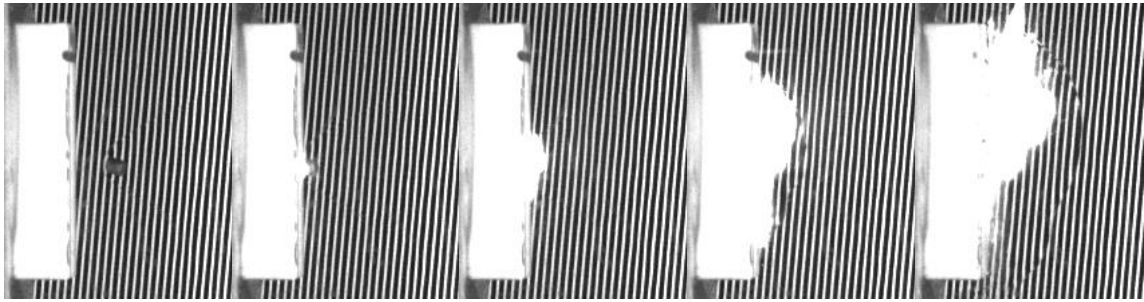
Fig. 2 Mg impact in Ar – O₂ 21% at 1.3 km/s, 200 ns exposure and 1 Mfps (frames 17, 24, 26, 34, 51)

Fig. 3 shows the Mach number as a function of distance from the target for all the Al impacts. Discrepancies between impact tests performed in the same atmosphere at the same impact speed can be attributed to the different tilt angles of the projectile before impact. Nonetheless, the same trend is observed among the different metals, i.e., the Mach number increases with oxygen concentration. More specifically, there appears to be a critical oxygen concentration threshold at which the blast wave Mach number increases significantly. The Mach number decay with distance for impacts in argon tends to be the smallest, followed by impacts in air, Ar – O₂ 21 %, and Ar – O₂ 30 % all together. The jump in Mach number occurred with an increase in the oxygen concentration from 30 % to 40 %.

The deceleration of the blast wave with distance appears to be independent of the atmosphere. Thus, at least for the duration of the recordings (126 μs maximum), the post-impact energy release does not influence the horizontal speed of the blast wave at the level of the impact point.
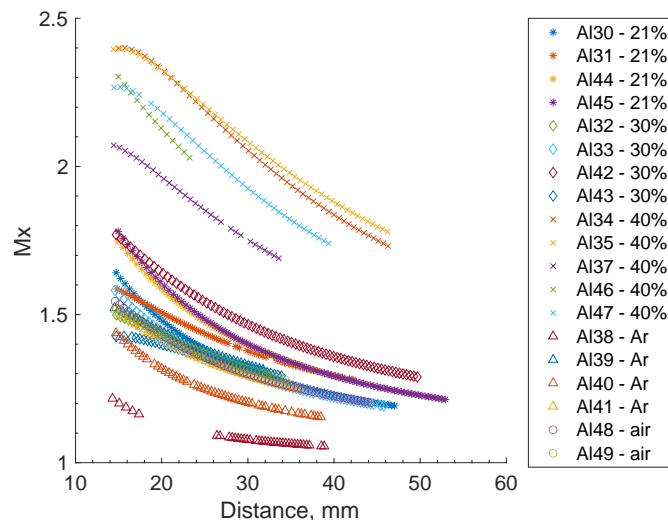

Fig. 3 Mach number as a function of distance from the target for Al impact tests performed in Ar, Ar – O₂ 21%, Ar – O₂ 30%, Ar – O₂ 40%, and air at impact speeds ~ 1.2 km/s.

Imaging pyrometry was performed for Al and Zr projectiles in all atmospheres. Fig. 4 shows the temperature map obtained for an aluminum impact in Ar – O₂ 40%. Image superposition is shown (left image), followed by thresholding applied to remove pixels below a certain intensity (center image), and the temperature map (right image). The mean of the temperature distribution is near 3300 K. Fig. 4 is a typical representation of the results obtained in all the other oxidizing atmospheres. Results showed that the temperature of the fine particles shed during impact in all the oxidizing atmospheres is slightly less than the predicted adiabatic flame temperature in air at standard conditions (~ 3500 K and ~ 3800 K for Al and Zr, respectively). The particles shed burn in the diffusion-limited regime in all oxidizing atmospheres. Thus, the jump in Mach number observed with the oxygen concentration increased to 40

% cannot be explained by a change in the chemical kinetics, which is temperature dependent, but rather a change in diffusion rates, i.e., the oxygen concentration must have an influence on the reaction rate via diffusion. The reaction rate in $Ar - O_2$ 40% must be high enough to ensure coupling between the energy release and the blast wave during the early-impact stage.

In future work, we intend on estimating the reaction rate threshold that permits energy coupling to the blast wave.
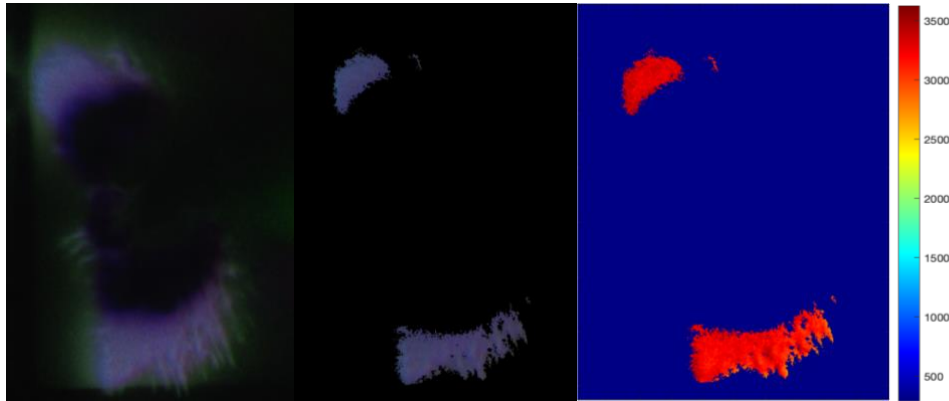

Fig. 4 Result from three-colour imaging pyrometry of an Al impact in $Ar - O_2$ 40% at ~ 1.2 km/s. (Left) Image superposition after applying the transformation matrices. (Center) Intensity thresholding is applied to remove pixels below a certain intensity (10 – 20 % of the maximum 2^{16}). (Right) Temperature map with the mean of the distribution at 3300 K. The image was captured 2 μs after contact between the projectile and the target. A 200 ns exposure time was used.

References

[1] Idrici D, Goroshin S, Soo MJ, Frost DL. (2021). Light emission signatures from ballistic impact of reactive metal projectiles. International Journal of Impact Engineering. 150, 103814

[2] Ames RG. (2007). A Standardized Evaluation Technique for Reactive Warhead Fragments. 23rd International Symposium on Ballistics. 49 – 58.

[3] McNesby K, Dean S, Benjamin R, Densmore J. (2021). Imaging pyrometry for most color cameras using a triple pass filter. Review of Scientific Instruments. 92, 063102

[4] Densmore J, Homan B, McNesby K. (2011). High-speed two-camera imaging pyrometer for mapping fireball temperatures. Applied Optics. 50, 6267 – 6271

[5] Goroshin S, Frost D, Levine J, Yoshinaka A, Zhang F. (2006). Optical pyrometry of fireballs of metalized explosives. Propellants, Explosives, Pyrotechnics. 31, 169 – 181.

[6] Densmore J, Biss M, Homan B, McNesby K. (2012). Thermal imaging of nickel-aluminum and aluminum-polytetrafluoroethylene impact initiated combustion. Journal of Applied Physics. 112

[7] Kleine H, Dewey J, Ohashi K, Mizukaki T, Takayama K. (2003). Studies of the TNT equivalence of silver azide charges. Shock Waves. 13, 123 – 138